Modulating charge density wave states in $TaSe_2$ by an electride substrate

Xiao-Le Qiu, Jian-Feng Zhang, Ben-Chao Gong, Huan-Cheng Yang, Zhong-Yi Lu,* and Kai Liu†
Department of Physics and Beijing Key Laboratory of Opto-electronic Functional Materials & Micro-nano Devices, Renmin University of China, Beijing 100872, China

(Received 15 July 2021; revised 17 September 2021; accepted 22 September 2021; published 5 October 2021)

Modulating charge density wave (CDW) states in layered materials has both fundamental scientific value and application potential in future electronic devices. Based on first-principles electronic structure calculations, we have studied the modulation of the CDW states in $TaSe_2$ by using a typical electride Ca_2N as the substrate. We find that the Ca_2N monolayer can donate 0.49 electrons/f.u. to the $TaSe_2$ monolayer and meanwhile avoids the disorder effect in conventional chemical substitution approach. With the uniform electron doping from Ca_2N, the CDW order in 1*H*-$TaSe_2$ is completely suppressed; in comparison, the CDW period in 1*T*-$TaSe_2$ transforms from the Star of David pattern to a $\sqrt{3} \times \sqrt{3}$ triangular pattern. Our studies enrich the phase diagram of $TaSe_2$ and highlight the effective manipulation of the CDW states via an electride substrate, which calls for future experimental verification.

DOI: 10.1103/PhysRevB.104.165109

I. INTRODUCTION

The charge density wave (CDW) states in real materials, which are characterized by a periodic modulation of the electron densities and the atomic positions with a wave vector $\mathbf{Q}_{\mathrm{CDW}}$ [1], have attracted extensive attention for decades. The exploration of a CDW state can improve our understanding of the superconductivity mechanism [2,3] due to the adjacency of the CDW and superconducting states [4], and CDW states also have potential applications in electronic devices such as logic circuits [5], nonvolatile memory [6–8], photodetector [9], and CDW-based oscillator [10]. As a typical CDW material, the transition metal dichalcogenide $TaSe_2$ has layered 2*H* and 1*T* phases in bulk form, which both undergo CDW transitions with decreasing temperature. Here, 2*H*-$TaSe_2$ shows an incommensurate CDW transition at 120 K, followed by a commensurate CDW transition with a 3×3 lattice deformation at 90 K [11], and finally, a superconducting transition at 0.2 K [12]. In comparison, 1*T*-$TaSe_2$ experiences an incommensurate CDW transition <600 K and a commensurate CDW transition with the Star of David pattern at 473 K [13]. Recently, the successful exfoliation of 2*H*- and 1*T*-$TaSe_2$ down to atomic layers provided an opportunity to study the dimensionality effect on the CDW states [13,14]. A Raman spectroscopy study on monolayer and bilayer 2*H*-$TaSe_2$ revealed the phonon mode softening due to electron-phonon coupling, which is associated with the incommensurate CDW phase transition [13]. A combined experimental and theoretical study confirmed that the reduction of dimension has no significant effect on the 3×3 CDW state of 2*H*-$TaSe_2$ [15]. Nevertheless, the calculated electron-phonon coupling (EPC) of monolayer 1*H*-$TaSe_2$ is largely enhanced, resulting in an increase of superconducting T_c to 2.2 K [16]. For 1*T*-$TaSe_2$, the transition temperature of commensurate CDW is reduced with the decreasing film thickness [17]. More interestingly, the monolayer 1*T*-$TaSe_2$ exhibits a Mott insulator behavior [18–20]. The prominent temperature and dimensionality effects on the CDW states of $TaSe_2$ suggest that $TaSe_2$ can serve as a prototype for studying the CDW-related physics.

Beyond the temperature and dimensionality effects, other approaches have also been adopted to tune the CDW states in $TaSe_2$. For 2*H*-$TaSe_2$, the intercalation of alkali metal ions [21–23] can change the band structure and suppress the CDW state, while the photoexcitation can drive the commensurate CDW state to a normal metallic state [24]. As to 1*T*-$TaSe_2$, the pressure can suppress the CDW distortion [25], and an ultrafast laser pulse can excite a long-lived metastable CDW state [26]. Moreover, the strain also has great influence on the CDW state [27–29]. A recent study reported that the tensile strain can suppress the CDW order of monolayer 1*H*-$TaSe_2$, while the compressive strain will enhance it [27]. On the other hand, the CDW state can be altered by constructing heterostructures. A recent experiment showed that, in the 1*T*-TaS_2/black phosphorus heterostructure, the transition temperature of the CDW states from nearly commensurate to commensurate was reduced to 4.5 K, lower than the original 180 K [30]. Black phosphorus is a semiconductor with a smaller work function (WF) than that of TaS_2 [30,31], indicating the occurrence of electron transfer [30]. Therefore, it is natural to ask whether there are some layered materials with low WFs that can interact strongly with $TaSe_2$ and modulate its CDW states.

The two-dimensional (2D) electrides are likely such materials with low WFs. As a typical electride, Ca_2N has been successfully synthesized in bulk form [32,33] and can be further exfoliated to the ultrathin limit [34]. Bulk Ca_2N has a WF of 2.6 eV [32] and can be written as $[Ca_2N]^+ \cdot e^-$ due to the remaining electrons between layers, while monolayer Ca_2N

*zlu@ruc.edu.cn
†kliu@ruc.edu.cn

with a free-electron gas floating on the surface can serve as an electron donor [35]. Compared with the commonly used doping methods such as alkali metal doping [36], Li-intercalation [21], and organic molecular functionalization [37] that hardly achieve a high doping density of $\sim 10^{14}$ cm^{-2}, Ca_2N can donate a carrier concentration up to 5×10^{14} cm^{-2} [38], which is on the same order of magnitude as the ionic gating technique [39]. Hence, it is interesting to investigate the effect of the electride Ca_2N as a substrate to tune the CDW states in $TaSe_2$.

In this paper, we study the atomic structures and the electronic properties of the $TaSe_2/Ca_2N$ heterostructures by using density functional theory (DFT) calculations. We find that the electron doping from Ca_2N can suppress the CDW order in $1H$-$TaSe_2$ and alter the CDW period in $1T$-$TaSe_2$, respectively. These findings enrich the phase diagram of $TaSe_2$ and suggest an electride as an ideal substrate to modulate a quantum state via uniform charge doping.

II. COMPUTATIONAL DETAILS

To study the atomic structures and the electronic properties of $TaSe_2/Ca_2N$ heterostructures, DFT calculations were performed with the projector augmented wave method [40,41] as implemented in the Vienna *Ab initio* Simulation Package (VASP) [42–44]. The generalized gradient approximation in the scheme of Perdew-Burke-Ernzerhof [45] was applied for the exchange correlation functional. The cutoff energy of the plane-wave basis was set to 520 eV. A vacuum space >20 Å was adopted to eliminate the interactions between the image heterostructures. The DFT-D2 method [46,47] was used to describe the van der Waals interaction between the Ca_2N and $TaSe_2$ layers. The $12 \times 12 \times 1$ and $6 \times 6 \times 1$ Monkhorst-Pack **k**-point meshes were adopted to sample the Brillouin zones (BZs) of the unit cell and the supercell, respectively. The Fermi surface was broadened by the Gaussian smearing method with a width of 0.05 eV. The internal atomic positions and the cell parameters were fully optimized until the residual forces on atoms were <0.01 eV/Å. The energy convergence criterion was set to 10^{-6} eV. The spin-orbit coupling effect was included in the band structure and the density of states (DOS) calculations. The phonon dispersion was calculated based on a supercell approach by using the PHONOPY code [48]. A $6 \times 6 \times 1$ supercell with a $4 \times 4 \times 1$ **k**-point mesh was used for the phonon calculations of the unit-cell of the $TaSe_2/Ca_2N$ heterostructure, while a $2\sqrt{3} \times 2\sqrt{3} \times 1$ supercell with a $4 \times 4 \times 1$ **k**-point mesh was used for those of the $\sqrt{3} \times \sqrt{3}$ supercell of the $1T$-$TaSe_2/Ca_2N$ heterostructure. The binding energy E_b was obtained according to the formula $E_b = E_{hetero} - E_{Ca_2N} - E_{TaSe_2}$, where E_{hetero} is the energy of the $TaSe_2/Ca_2N$ heterostructure, and E_{Ca_2N} (E_{TaSe_2}) is the energy of monolayer Ca_2N ($TaSe_2$).

III. RESULTS AND ANALYSIS

The crystal structures of monolayers Ca_2N, $1H$-$TaSe_2$, and $1T$-$TaSe_2$ are shown in Fig. 1. They all have sandwiched structures with the same kinds of atoms at the top and bottom surfaces. The normal phases of Ca_2N and $1T$-$TaSe_2$ have the point group symmetry of D_{3d}, while that of $1H$-$TaSe_2$ is D_{3h}.

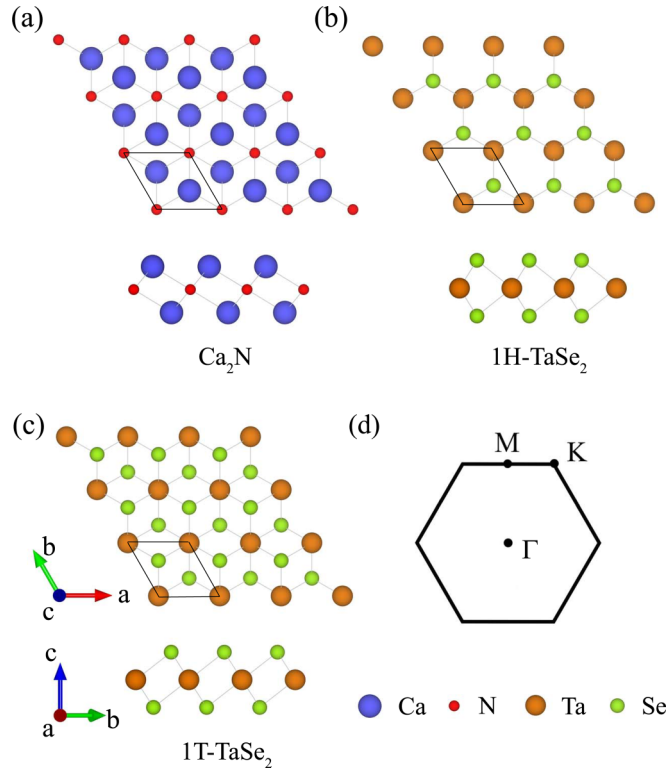

FIG. 1. Top and side views of (a) Ca_2N, (b)$1H$-$TaSe_2$, and (c) $1T$-$TaSe_2$ monolayers. The blue, red, orange, and green balls represent Ca, N, Ta, and Se atoms, respectively. (d) Two-dimensional Brillouin zone (BZ) of the unit cell.

Our calculated in-plane lattice constants of Ca_2N (3.57 Å), $1H$-$TaSe_2$ (3.49 Å), and $1T$-$TaSe_2$ (3.55 Å) are in good accordance with previous studies [18,49,50]. The respective lattice mismatches of $1H$-$TaSe_2/Ca_2N$ and $1T$-$TaSe_2/Ca_2N$ are only 2.3 and 0.5%, indicating the possibility of ideal heterostructure construction. We first study the atomic and electronic structures of the $1H$-$TaSe_2/Ca_2N$ heterostructure. To obtain the most stable stacking structure, six possible configurations labeled from H-1 to H-6 were considered (see Fig. 5 in the Appendix). The H-1 structure is obtained by directly stacking $1H$-$TaSe_2$ above Ca_2N with the Se atoms on top of the upper Ca atoms and the Ta atoms on top of the N atoms. The H-2 (H-3) structure is constructed by shifting the $1H$-$TaSe_2$ layer in the H-1 structure by one (two) third(s) of the unit cell along the diagonal line. The H-4 structure is obtained by rotating the $1H$-$TaSe_2$ layer in the H-1 structure by 180°, while the H-5 (H-6) structure is constructed by shifting the $1H$-$TaSe_2$ layer in the H-4 structure by one (two) third(s) of the unit cell along the diagonal line. The energy differences among these heterostructures are listed in Table I. Overall,

TABLE I. The energy differences (meV/f.u.) among the six configurations of $1H$-$TaSe_2/Ca_2N$ heterostructures. The energy of the H-2 structure is set to zero.

Structure	H-1	H-2	H-3	H-4	H-5	H-6
ΔE	939	0	199	77	121	695

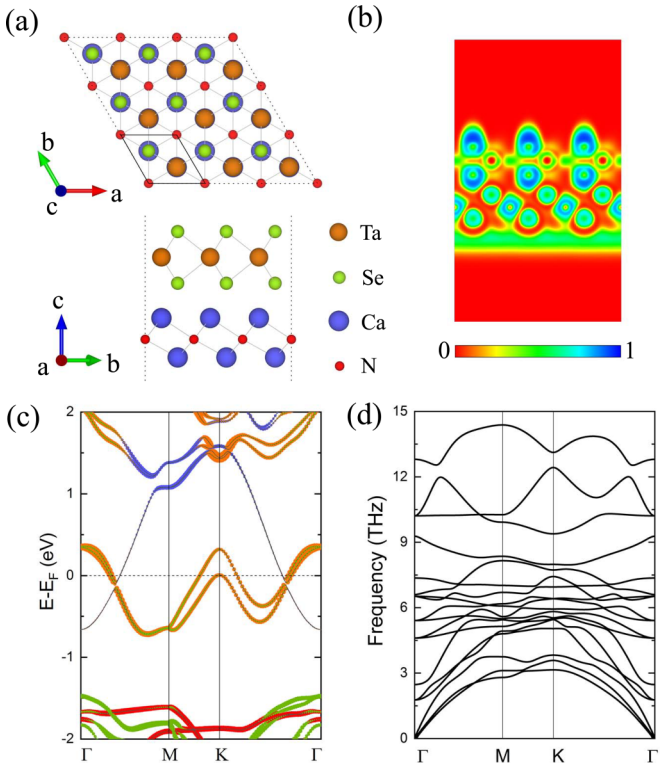

FIG. 2. (a) Top and side views of the optimized 1H-$TaSe_2/Ca_2N$ heterostructure. The unit cell is outlined by the black solid line. (b) Electron localization function (ELF) map for the side view of the 1H-$TaSe_2/Ca_2N$ heterostructure. The 0 and 1 values represent the completely delocalized and localized electrons, respectively. (c) Electronic band structure and (d) phonon dispersion of the 1H-$TaSe_2/Ca_2N$ heterostructure along the high-symmetry paths of the BZ. The sizes of the blue, red, orange, and green dots in the electronic band structure represent the orbital weights of Ca, N, Ta, and Se atoms, respectively.

the H-2 structure [Fig. 2(a)] is energetically the most stable one, which is at least 77 meV/f.u. in energy lower than the other structures. We hence focus on the H-2 structure in the following.

The atomic structure of the most stable 1H-$TaSe_2/Ca_2N$ heterostructure, i.e., the H-2 structure, is displayed in Fig. 2(a). It has an in-plane lattice constant of 3.55 Å and an interlayer distance of 2.20 Å. While the ideal Ca_2N monolayer has free electron gas floating on both surfaces [51], dramatic changes take place in the charge distribution of the 1H-$TaSe_2/Ca_2N$ heterostructure. From the electron localization function (ELF) map shown in Fig. 2(b), it can be seen clearly that the free electron gas between the two layers disappears, and only the electron gas on the bottom surface of Ca_2N remains. Based on the Bader charge analysis, we find that there are ∼0.49 electrons/f.u. transferred from Ca_2N to 1H-$TaSe_2$, which results from the low WF (2.6 eV) [32] of Ca_2N. Figure 2(c) demonstrates the calculated band structure of the 1H-$TaSe_2/Ca_2N$ heterostructure, in which the electronic bands around the Fermi level are mainly contributed by the Ta-d and Se-p orbitals. A previous study has shown that monolayer 1H-$TaSe_2$ has a 3 × 3 CDW pattern formed by the triangular clustering of Ta atoms [13]. It is thus interesting to

TABLE II. The energy differences (meV/f.u.) among the six configurations of 1T-$TaSe_2/Ca_2N$ heterostructures. The energy of the T-3 structure is set to zero.

Structure	T-1	T-2	T-3	T-4	T-5	T-6
ΔE	204	637	0	634	76	118

examine the CDW state in the 1H-$TaSe_2/Ca_2N$ heterostructure. From the calculated phonon dispersion [Fig. 2(d)], there is no imaginary phonon mode across the BZ, indicating dynamical stability. To distinguish the effects of charge doping and lattice strain on the CDW state of 1H-$TaSe_2$ induced by the Ca_2N substrate, we have also calculated the phonon spectrum by fixing the in-plane lattice constant to 3.49 Å, which corresponds to the free-standing 1H-$TaSe_2$ monolayer. We find that the 1H-$TaSe_2/Ca_2N$ heterostructure still has no soft modes, suggesting that charge doping plays a major role here. In comparison, a previous study indicated that, without the Ca_2N substrate, the electron doping enhances the CDW instability of the 1H-$TaSe_2$ monolayer, while the tensile strain suppresses it [27]. These results suggest that Ca_2N can construct a stable heterostructure with 1H-$TaSe_2$ and completely suppress the CDW order of the latter via the uniform electron doping. The phonon dispersions of other structures in Table I except the H-2 structure are shown in Figs. 7(a)–7(e) in the Appendix. Like the case of the H-2 structure, there are no imaginary phonon modes in the whole BZ for H-3, H-4, and H-5 structures, which means that the CDW order is also suppressed in these 1H structures. Meanwhile, the H-1 and H-6 configurations have imaginary phonon modes around the Γ point, which correspond to the two highest-energy structures (Table I).

We next consider the 1T-$TaSe_2/Ca_2N$ heterostructure. Like the case of 1H-$TaSe_2/Ca_2N$, we constructed six different configurations labeled from T-1 to T-6 (see Fig. 6 in the Appendix). From the energy differences among these six configurations listed in Table II, we learn that the T-3 structure is the most stable stacking configuration, which is at least 76 meV/f.u. in energy lower than other structures. Therefore, for the 1T-$TaSe_2/Ca_2N$ heterostructure, we will focus on the T-3 structure in the following.

Figure 3(a) displays the top and side views of the optimized 1T-$TaSe_2/Ca_2N$ heterostructure (the T-3 structure). The relaxed in-plane lattice constant (3.58 Å) and interlayer distance (2.20 Å) are like those of the 1H-$TaSe_2/Ca_2N$ heterostructure. From the ELF map shown in Fig. 3(b), we can see that the free electron gas floating on the top surface of Ca_2N also disappears. There are ∼0.47 electrons/f.u. transferred from Ca_2N to 1T-$TaSe_2$ according to the Bader charge analysis. The 1T-$TaSe_2$ monolayer was reported to enter a CDW phase with the Star of David pattern at low temperature [52]. We hence calculated the phonon dispersion of the 1T-$TaSe_2/Ca_2N$ heterostructure. There exist imaginary phonon modes in the BZ [Fig. 3(c)], indicating the structural instability. The largest imaginary mode appears around the K point, which is however different from the $\mathbf{Q}_{CDW}$ vector for the Star of David pattern of monolayer 1T-$TaSe_2$ [20]. From the inset of Fig. 4(a), we can see that the K point in the unit cell BZ can be folded to

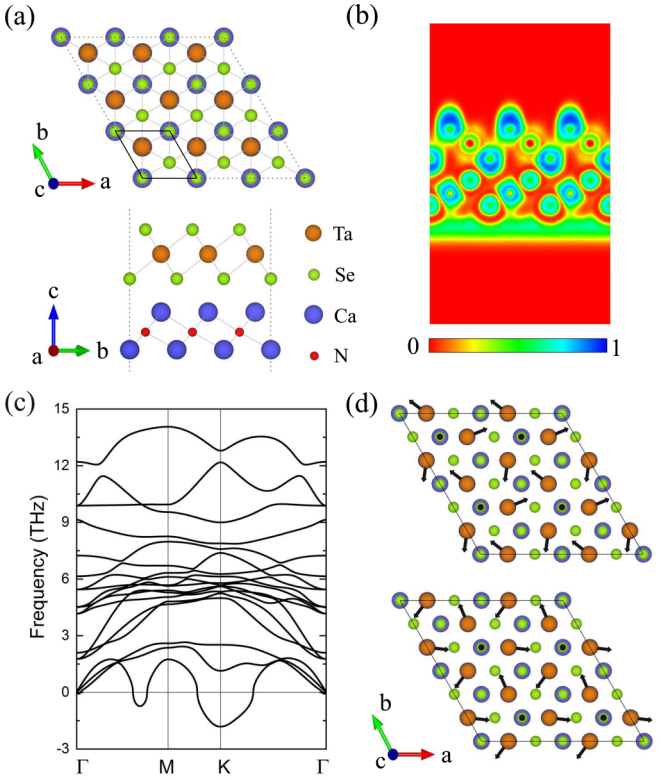

FIG. 3. (a) Top and side views of the optimized 1T-$TaSe_2/Ca_2N$ heterostructure. The unit cell is outlined by the black solid line in the top view. (b) ELF map for the side view of the 1T-$TaSe_2/Ca_2N$ heterostructure. (c) Phonon dispersion of the 1T-$TaSe_2/Ca_2N$ heterostructure along the high-symmetry paths of the BZ. (d) Displacement patterns of two doubly degenerated imaginary phonon modes at the K point of the unit cell BZ [the Γ point in the BZ of the $\sqrt{3} \times \sqrt{3}$ supercell in Fig. 4(a)].

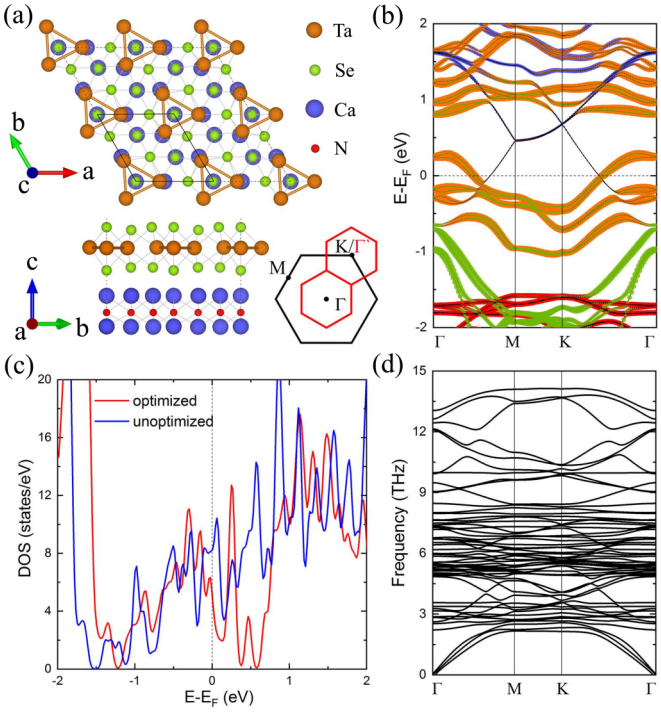

FIG. 4. (a) Top and side views of the optimized $\sqrt{3} \times \sqrt{3}$ supercell of the 1T-$TaSe_2/Ca_2N$ heterostructure. The $\sqrt{3} \times \sqrt{3}$ supercell is outlined by the black solid line in the top view. The BZs of the unit cell (black) and the $\sqrt{3} \times \sqrt{3}$ supercell (red) are shown in the right corner, while the K point in the former one coincides with the Γ point in the latter one. (b) Electronic band structures along the high-symmetry paths of the two-dimensional (2D) BZ for the $\sqrt{3} \times \sqrt{3}$ supercell. The sizes of the blue, red, orange, and green dots represent the orbital weights of Ca, N, Ta, and Se atoms, respectively. (c) Density of states (DOS) of the optimized and unoptimized heterostructures in the $\sqrt{3} \times \sqrt{3}$ supercell. (d) Phonon dispersion of the optimized $\sqrt{3} \times \sqrt{3}$ supercell.

the BZ center of the $\sqrt{3} \times \sqrt{3}$ supercell. We thus plot the displacement patterns of the maximum imaginary modes at the latter **k** point, which mainly come from the vibrations of Ta atoms and tend to form triangular clusters [Fig. 3(d)]. We also tested the stability of other structures in Table II. They all have large imaginary phonon modes at the K point, indicating a structural reconstruction like the case of the T-3 structure. After optimizing the structures of Table II with the $\sqrt{3} \times \sqrt{3}$ supercells, the T-3 structure still possesses the lowest energy.

The fully relaxed structure for the $\sqrt{3} \times \sqrt{3}$ supercell of the 1T-$TaSe_2/Ca_2N$ heterostructure (T-3) is shown in Fig. 4(a). The Ta-Ta bonds with lengths <3.4 Å are marked as orange sticks in the top view. Obviously, these Ta atoms form triangular clusters after structural optimization. The in-plane lattice constant and the interlayer distance are 6.20 and 2.03 Å, respectively. Compared with the unit cell structure in Fig. 3(a), the interlayer distance is reduced by 0.17 Å. These structural reconstructions enhance the binding energy between the 1T-$TaSe_2$ and Ca_2N layers from −0.46 to −0.55 eV/f.u. According to the phonon dispersion shown in Fig. 4(d), there is no imaginary phonon mode for the optimized structure of the $\sqrt{3} \times \sqrt{3}$ supercell. This indicates that, with the Ca_2N electride as a substrate, the CDW order in 1T-$TaSe_2$ changes from the original Star of David pattern to a new triangular pattern with the $\sqrt{3} \times \sqrt{3}$ period. Notably, this structure is like the $\sqrt{3} \times \sqrt{3}$ supercell of the 1T-MoS_2 monolayer [53], which also has imaginary phonon modes at the K point and shows the same displacement vectors as in Fig. 3(d). Figure 4(c) demonstrates the DOSs for the unoptimized and optimized $\sqrt{3} \times \sqrt{3}$ supercells. After the optimization, the DOS at the Fermi level drops steeply, which is consistent with the characteristics of the CDW phase transition. From the band structure of the optimized 1T-$TaSe_2/Ca_2N$ heterostructure shown in Fig. 4(b), we learn that the bands around the Fermi level are dominated by the Ta-d and Se-p orbitals. Based on the Bader charge analysis, there are 0.49 electrons/f.u. transferred from Ca_2N to $TaSe_2$ for the relaxed $\sqrt{3} \times \sqrt{3}$ supercell, like the case of 1H-$TaSe_2/Ca_2N$. The electron doping induced by the Ca_2N electride substrate is thus responsible for the CDW phase transition in 1T-$TaSe_2$.

IV. DISCUSSION AND SUMMARY

To explain the origin of the CDW order in real materials, several viewpoints such as the Peierls transition, the Fermi surface nesting, the EPC, and the exciton condensation have been proposed. The Peierls transition and the Fermi

surface nesting are often adopted to explain the electron redistribution accompanied by a periodic lattice distortion in quasi-one-dimensional systems [54]. As to the CDW states in quasi-two-dimensional transition metal dichalcogenides, the momentum-dependent EPC may play a major role. For example, angle-resolved photoemission spectroscopy investigations [55] showed the absence of Fermi surface nesting in $2H$-$NbSe_2$, while inelastic x-ray measurements confirmed that EPC determines the CDW order [56]. Similarly, the periodic lattice distortions in $1T$-$TaSe_2$ and monolayer $1T$-VSe_2 can be understood in the framework of the momentum-dependent EPC [57,58]. Nevertheless, the origin of the CDW ordering in $1T$-$TiSe_2$ is under debate, while recently the exciton condensation mechanism [59–61] and both the contributions from exciton pairing and EPC [62] were proposed. In our above calculations on $TaSe_2/Ca_2N$, we find that the electron doping from Ca_2N can completely suppress the CDW order in $1H$-$TaSe_2$ [Fig. 2(d)] but cannot generate the superconductivity in their heterostructure, even though either $TaSe_2$ or Ca_2N is superconducting [16,63]. This may result from the heavily released EPC in the $1H$-$TaSe_2/Ca_2N$ stacking structure. As for the $1T$-$TaSe_2/Ca_2N$ heterostructure, the induced $\sqrt{3} \times \sqrt{3}$ CDW pattern is apparently related to the phonon softening around the K point of the BZ [Fig. 3(c)]. Since previous studies have found that Cu doping in $1T$-$TiSe_2$ [64] and $2H$-$TaSe_2$ [65] can suppress the CDW state and induce/enhance the superconductivity, whether the heterostructure composed of $TaSe_2$ and electride can be tuned to superconducting needs further exploration.

In summary, we have studied the atomic and electronic structures of the heterostructures composed of a transition metal dichalcogenide $TaSe_2$ and an electride Ca_2N based on DFT calculations. We find that the charge transfer from Ca_2N to $TaSe_2$ has a significant influence on the CDW order of the latter. The CDW order in $1H$-$TaSe_2$ is completely suppressed, while for $1T$-$TaSe_2$, there is a CDW phase transition from the original Star of David pattern with a $\sqrt{13} \times \sqrt{13}$ period to a triangular pattern with a $\sqrt{3} \times \sqrt{3}$ period. These results indicate that electrides can serve as ideal substrates with uniform electron doping to modulate the CDW states in layered materials and have great potential to tune other ordering states in quantum materials.

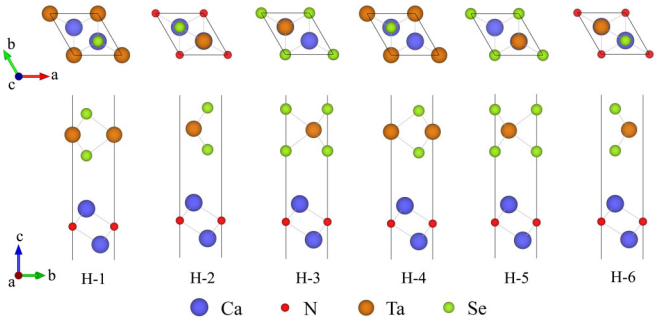

FIG. 5. Top and side views of the $1H$-$TaSe_2/Ca_2N$ heterostructure. The six configurations are labeled as H-1 to H-6. The blue, red, orange, and green balls represent the Ca, N, Ta, and Se atoms, respectively.

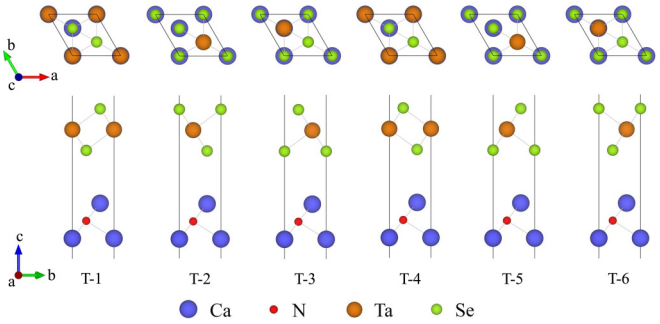

FIG. 6. Top and side views of the $1T$-$TaSe_2/Ca_2N$ heterostructure. The six configurations are labeled as T-1 to T-6.

ACKNOWLEDGMENTS

This paper was supported by the Beijing Natural Science Foundation (Grant No. Z200005), the National Key R&D Program of China (Grants No. 2017YFA0302903 and No. 2019YFA0308603), the National Natural Science Foundation of China (Grants No. 11774424 and No. 11934020), the CAS Interdisciplinary Innovation Team, the Fundamental Research Funds for the Central Universities (CN), and the Research Funds of Renmin University of China (Grants No. 19XNLG13 and No. 20XNH064). Computational resources were provided by the Physical Laboratory of High Performance Computing at Renmin University of China.

APPENDIX

The top and side views for the possible stacking configurations of the $1H$-$TaSe_2/Ca_2N$ (Fig. 5) and the $1T$-$TaSe_2/Ca_2N$ (Fig. 6) heterostructures. According to our calculations, the H-2 and T-3 are energetically the most stable ones in the respective heterostructures. The calculated phonon dispersions for all other structures in Tables I and II except the H-2 and T-3 structures are shown in Fig. 7. Even after the relaxation in larger supercells, the H-2 and T-3 structures still have the lowest energies for the $1H$-$TaSe_2/Ca_2N$ and $1T$-$TaSe_2/Ca_2N$ heterostructures, respectively.

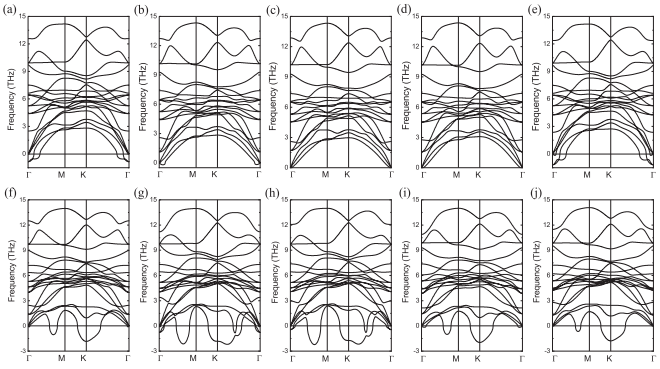

FIG. 7. (a)–(e) Phonon dispersions of the H-1, H-3, H-4, H-5, and H-6 configurations of the $1H$-$TaSe_2/Ca_2N$ heterostructures, respectively. (f)–(j) Phonon dispersions of the T-1, T-2, T-4, T-5, and T-6 configurations of the $1T$-$TaSe_2/Ca_2N$ heterostructures, respectively.

[1] R. H. Friend and D. Jerome, J. Phys. C: Solid State Phys. **12**, 1441 (1979).
[2] A. H. Castro Neto, Phys. Rev. Lett. **86**, 4382 (2001).
[3] A. M. Gabovich, A. I. Voitenko, and M. Ausloos, Phys. Rep. **367**, 583 (2002).
[4] Y. Liu, R. Ang, W. J. Lu, W. H. Song, L. J. Li, and Y. P. Sun, Appl. Phys. Lett. **102**, 192602 (2013).
[5] A. G. Khitun, A. K. Geremew, and A. A. Balandin, IEEE Electron Device Lett. **39**, 1449 (2018).
[6] M. Yoshida, R. Suzuki, Y.-J. Zhang, M. Nakano, and Y. Iwasa, Sci. Adv. **1**, e1500606 (2015).
[7] M. Yoshida, T. Gokuden, R. Suzuki, M. Nakano, and Y. Iwasa, Phys. Rev. B **95**, 121405(R) (2017).
[8] Y. Sun, T. Dai, Z.-H. He, W.-Q. Zhou, P. Hu, S. W. Li, and S.-X. Wu, Appl. Phys. Lett. **116**, 033101 (2020).
[9] Y. H. Huang, R. S. Chen, J. R. Zhang, and Y. S. Huang, Nanoscale **7**, 18964 (2015).
[10] G.-X. Liu, B. Debnath, T. R. Pope, T. T. Salguero, R. K. Lake, and A. A. Balandin, Nat. Nanotechnol. **11**, 845 (2016).
[11] J. Wilson, F. J. D. Salvo, and S. Mahajan, Adv. Phys. **24**, 117 (1975).
[12] T. Kumakura, H. Tan, T. Handa, M. Morishita, and H. Fukuyama, Czech. J. Phys. **46**, 2611 (1996).
[13] P. Hajiyev, C.-X. Cong, C.-Y. Qiu, and T. Yu, Sci. Rep. **3**, 2593 (2013).
[14] H. Li, G. Lu, Y. Wang, Z. Yin, C. Cong, Q. He, L. Wang, F. Ding, T. Yu, and H. Zhang, Small **9**, 1974 (2013).
[15] H. Ryu, Y. Chen, H. Kim, H.-Z. Tsai, S. Tang, J. Jiang, F. Liou, S. Kahn, C. Jia, A. A. Omrani, J. H. Shim, Z. Hussain, Z.-X. Shen, K. Kim, B. I. Min, C. Hwang, M. F. Crommie, and S.-K. Mo, Nano Lett. **18**, 689 (2018).
[16] C.-S. Lian, C. Heil, X. Liu, C. Si, F. Giustino, and W.-H. Duan, J. Phys. Chem. Lett. **10**, 4076 (2019).
[17] R. Samnakay, D. Wickramaratne, T. R. Pope, R. K. Lake, T. T. Salguero, and A. A. Balandin, Nano Lett. **15**, 2965 (2015).
[18] Y. Nakata, T. Yoshizawa, K. Sugawara, Y. Umemoto, T. Takahashi, and T. Sato, ACS Appl. Nano Mater. **1**, 1456 (2018).
[19] P. Darancet, A. J. Millis, and C. A. Marianetti, Phys. Rev. B **90**, 045134 (2014).
[20] K. Zhang, C. Si, C.-S. Lian, J. Zhou, and Z.-M. Sun, J. Mater. Chem. C **8**, 9742 (2020).
[21] Y.-S. Wu, H. Xing, C.-S. Lian, H. L. Lian, J.-M. He, W.-H. Duan, J.-Y. Liu, Z.-Q. Mao, and Y. Liu, Phys. Rev. Mater. **3**, 104003 (2019).
[22] H. E. Brauer, H. I. Starnberg, L. J. Holleboom, H. P. Hughes, and V. N. Strocov, J. Phys.: Condens. Matter **13**, 9879 (2001).
[23] A. König, K. Koepernik, R. Schuster, R. Kraus, M. Knupfer, B. Büchner, and H. Berger, Europhys. Lett. **100**, 27002 (2012).
[24] P.-F. Zhu, J. Cao, Y. Zhu, J. Geck, Y. Hidaka, S. Pjerov, T. Ritschel, H. Berger, Y. Shen, R. Tobey, J. P. Hill, and X. J. Wang, Appl. Phys. Lett. **103**, 071914 (2013).
[25] Y. Z. Ge and A. Y. Liu, Phys. Rev. B **82**, 155133 (2010).
[26] X. Shi, W.-J. You, Y.-C. Zhang, Z.-S. Tao, P. M. Oppeneer, X.-X. Wu, R. Thomale, K. Rossnagel, M. Bauer, H. Kapteyn, and M. Murnane, Sci. Adv. **5**, eaav4449 (2019).
[27] J. G. Si, M. J. Wei, H. Y. Wu, R. C. Xiao, and W. J. Lu, Europhys. Lett. **127**, 37001 (2019).
[28] D. Svetin, I. Vaskivskyi, P. Sutar, E. Goreshnik, J. Gospodaric, T. Mertelj, and D. Mihailovic, Appl. Phys. Express **7**, 103201 (2014).
[29] R. Zhao, Y. Wang, D. Deng, X. Luo, W. J. Lu, Y.-P. Sun, Z.-K. Liu, L.-Q. Chen, and J. Robinson, Nano Lett. **17**, 3471 (2017).
[30] Z.-Y. Wang, L.-Q. Chu, L.-J. Li, M. Yang, J.-Y. Wang, G. Eda, and K. P. Loh, Nano Lett. **19**, 2840 (2019).
[31] Y.-Q. Cai, G. Zhang, and Y.-W. Zhang, Sci. Rep. **4**, 6677 (2014).
[32] K. Lee, S. W. Kim, Y. Toda, S. Matsuishi, and H. Hosono, Nature (London) **494**, 336 (2013).
[33] J. S. Oh, C.-J. Kang, Y. J. Kim, S. Sinn, M. Han, Y. J. Chang, B.-G. Park, S. W. Kim, B. I. Min, H.-D. Kim, and T. W. Noh, J. Am. Chem. Soc. **138**, 2496 (2016).
[34] D. L. Druffel, K. L. Kuntz, A. H. Woomer, F. M. Alcorn, J. Hu, C. L. Donley, and S. C. Warren, J. Am. Chem. Soc. **138**, 16089 (2016).
[35] Y. J. Kim, S. M. Kim, H. Hosono, J. W. Yang, and S. W. Kim, Chem. Commun. **50**, 4791 (2014).
[36] H. Fang, M. Tosun, G. Seol, T. C. Chang, K. Takei, J. Guo, and A. Javey, Nano Lett. **13**, 1991 (2013).
[37] D. Kiriya, M. Tosun, P. Zhao, J. S. Kang, and A. Javey, J. Am. Chem. Soc. **136**, 7853 (2014).
[38] T. Inoshita, M. Tsukada, S. Saito, and H. Hosono, Phys. Rev. B **96**, 245303 (2017).
[39] S. Z. Bisri, S. Shimizu, M. Nakano, and Y. Iwasa, Adv. Mater. **29**, 1607054 (2017).
[40] P. E. Blöchl, Phys. Rev. B **50**, 17953 (1994).
[41] G. Kresse and D. Joubert, Phys. Rev. B **59**, 1758 (1999).
[42] G. Kresse and J. Hafner, Phys. Rev. B **47**, 558(R) (1993).
[43] G. Kresse and J. Furthmüller, Comput. Mater. Sci **6**, 15 (1996).
[44] G. Kresse and J. Furthmüller, Phys. Rev. B **54**, 11169 (1996).
[45] J. P. Perdew, K. Burke, and M. Ernzerhof, Phys. Rev. Lett. **77**, 3865 (1996).
[46] X. Wu, M. C. Vargas, S. Nayak, V. Lotrich, and G. Scoles, J. Chem. Phys. **115**, 8748 (2001).
[47] S. Grimme, J. Comput. Chem. **27**, 1787 (2006).
[48] A. Togo, F. Oba, and I. Tanaka, Phys. Rev. B **78**, 134106 (2008).
[49] S. Guan, S.-Y., A. Yang, L.-Y. Zhu, J.-P. Hu, and Y.-G. Yao, Sci. Rep. **5**, 12285 (2015).
[50] D. C. Freitas, P. Rodière, M. R. Osorio, E. Navarro-Moratalla, N. M. Nemes, V. G. Tissen, L. Cario, E. Coronado, M. García-Hernández, S. Vieira, M. Núñez-Regueiro, and H. Suderow, Phys. Rev. B **93**, 184512 (2016).
[51] X.-L. Qiu, J.-F. Zhang, Z.-Y. Lu, and K. Liu, J. Phys. Chem. C **123**, 24698 (2019).
[52] P. C. Börner, M. K. Kinyanjui, T. Björkman, T. Lehnert, A. V. Krasheninnikov, and U. Kaiser, Appl. Phys. Lett. **113**, 173103 (2018).
[53] S. N. Shirodkar and U. V. Waghmare, Phys. Rev. Lett. **112**, 157601 (2014).
[54] X.-T. Zhu, J.-D. Guo, J.-D. Zhang, and E. W. Plummer, Adv. Phys. X **2**, 622 (2017).
[55] K. Rossnagel, O. Seifarth, L. Kipp, M. Skibowski, D. Voß, P. Krüger, A. Mazur, and J. Pollmann, Phys. Rev. B **64**, 235119 (2001).
[56] F. Weber, S. Rosenkranz, J.-P. Castellan, R. Osborn, R. Hott, R. Heid, K.-P. Bohnen, T. Egami, A. H. Said, and D. Reznik, Phys. Rev. Lett. **107**, 107403 (2011).
[57] Y. Liu, D. F. Shao, L. J. Li, W. J. Lu, X. D. Zhu, P. Tong, R. C. Xiao, L. S. Ling, C. Y. Xi, L. Pi, H. F. Tian, H. X. Yang, J. Q. Li,

W. H. Song, X. B. Zhu, and Y. P. Sun, Phys. Rev. B **94**, 045131 (2016).

[58] J. G. Si, W. J. Lu, H. Y. Wu, H. Y. Lv, X. Liang, Q. J. Li, and Y. P. Sun, Phys. Rev. B **101**, 235405 (2020).

[59] C. Monney, C. Battaglia, H. Cercellier, P. Aebi, and H. Beck, Phys. Rev. Lett. **106**, 106404 (2011).

[60] A. Kogar, M. S. Rak, S. Vig, A. A. Husain, F. Flicker, Y. I. Joe, L. Venema, G. J. MacDougall, T. C. Chiang, E. Fradkin, J. van Wezel, and P. Abbamonte, Science **358**, 1314 (2017).

[61] H. Cercellier, C. Monney, F. Clerc, C. Battaglia, L. Despont, M. G. Garnier, H. Beck, P. Aebi, L. Patthey, H. Berger, and L. Forró, Phys. Rev. Lett. **99**, 146403 (2007).

[62] C. Lian, S.-J. Zhang, S.-Q. Hu, M.-X. Guan, and S. Meng, Nat. Commun. **11**, 43 (2020).

[63] X.-Z. Zeng, S.-T. Zhao, Z.-Y. Li, and J.-L. Yang, Phys. Rev. B **98**, 155443 (2018).

[64] A. Bussmann-Holder and A. R. Bishop, Phys. Rev. B **79**, 024302 (2009).

[65] X. C. Li, M. H. Zhou, L. H. Yang, and C. Dong, Supercond. Sci. Technol. **30**, 125001 (2017).